Performance prediction of a multi-MW wind turbine adopting an advanced hydrostatic transmission

Paolo Silva [a], Antonio Giuffrida [a,*], Nicola Fergnani [a], Ennio Macchi [a], Matteo Cantù [b], Roberto Suffredini [b], Massimo Schiavetti [b], Gianluca Gigliucci [b]

[a] *Politecnico di Milano, Dipartimento di Energia, Via Lambruschini 4, 20156 Milano, Italy*
[b] *Enel Ingegneria e Ricerca SpA, Via Andrea Pisano 120, 56122 Pisa, Italy*

1. Introduction

The worldwide request for alternatives to fossil fuels has been growing considerably during the last decades, driving a rapid improvement of technologies exploiting renewable energies. Among them, there are wind energy conversion systems, mainly based on large-scale wind turbines using either a mechanical gearbox or a low-speed generator [1,2]. Both DFIG (doubly fed induction generator) wind turbines and direct-drive PMG (permanent magnet generator) wind turbines are widely used, nowadays. Low-speed PMG machines have higher reliability, compared to DFIG ones, owing to the elimination of the high-speed rotating components. As a matter of fact, the frequency converters for rotor speed variation and, in most cases, the mechanical gearbox are components that allow to obtain high overall efficiency in state-of-the-art multi-MW wind turbines, but are the main responsible for faults and out-of-service [3], causing high maintenance costs, especially in off-shore applications [4].

High-pressure fluid power systems, actually present in various applications such as fuel injection equipment [5], construction machinery [6], hybrid propulsion [7] and lubrication systems [8], could be used to replace some critical components of a wind energy conversion system. In particular, a hydrostatic transmission can link the rotor to the electric generator, combining good efficiency and grid stability with high reliability and relatively low costs. Recently, attention has been paid to solutions of hydrostatic transmissions integrated in wind turbine drive-trains, ranging from 100 kW [9] up to 1 MW [10] machines. Techno-economic feasibility studies for a proposed 1.5 MW wind turbine utilizing a continuously variable ratio hydrostatic drive-train were presented as well [11]. However, no matter how compact and robust they may be, state-of-the-art positive-displacement units currently present in hydrostatic transmissions really suffer from reduced efficiency at partial load and displacement volume different from the maximum, so energy transfer from the rotor to the electric generator could be seriously penalized. Digital fluid power is a recent branch that offers high potential for innovative solutions. A successful application requires new components, a sound understanding of the system and new control principles. Specific details about the state of the art can be found elsewhere [12], but in all cases, control is effected by switching valves. Digital fluid power offers several advantages compared with analog technologies, i.e. higher efficiency, precision, redundancy, robustness, as well as higher component

* Corresponding author.
  E-mail address: antonio.giuffrida@polimi.it (A. Giuffrida).

standardization potential [13]. As far as this study is concerned, digital-displacement pumps and motors [14] are selected as components of a high-efficiency hydrostatic transmission to be used in a wind energy conversion system in order to enhance its overall efficiency [15,16].

In the next sections, after presenting the basic principle of a hydrostatic transmission and its integration in a wind energy conversion system, details of wind turbine drive-train modeling and drive-train schemes are reported. Eventually, the results of the study are presented and discussed.

2. Hydrostatic transmission in a wind turbine drive-train

Hydrostatic transmissions are widely recognized as excellent systems for power transmission when variable output velocity is required in engineering applications, such as the fields of manufacturing, automation and heavy-duty vehicles. A hydrostatic transmission offers fast response, maintains precise velocity under varying loads and allows to control speed, torque, power or, in some cases, direction of rotation when required [17,18].

The operating principle of a hydrostatic transmission is simple: a positive-displacement pump, connected to the prime mover, generates a flow rate to drive a positive-displacement motor, which is connected to the load. If the displacement volumes of pump and motor are fixed, the hydrostatic transmission simply acts as a mechanical gearbox with fixed gear ratio that transmits power from the prime mover to the load. When using a variable-displacement pump or motor, or both, a continuous control of speed, torque and power is possible. Paying here attention to speed control, it is possible to formulate the theoretical flow rate generated by the pump, along with the theoretical rotational speed of the motor, by neglecting, for the sake of simplicity, leakage flows inside the machines [19]:

$$Q_{p,th} = \alpha_p \cdot V_p \cdot n_p \tag{1}$$

$$n_{m,th} = \frac{Q_m}{\alpha_m \cdot V_m} \tag{2}$$

If no fluid loss occurs in the hydraulic circuit, the whole flow rate generated by the pump enters the motor, so the rotational speeds of both pump and motor can be related:

$$n_{m,th} = \frac{\alpha_p \cdot V_p}{\alpha_m \cdot V_m} \cdot n_p \tag{3}$$

According to the last formula, a proper setting of pump and motor displacement volumes (by means of the factors α_p and α_m, variable from a minimum close to 0 up to 1) allows to control the rotational speed of the motor. This feature is interesting if a hydrostatic transmission has to be integrated in a wind turbine drive-train. Moreover, if advanced hydrostatic units based on the digital-displacement concept [14−16] are used, thanks to their high efficiency at both full- and partial-load conditions, it is possible to improve the overall energy conversion efficiency of the wind turbine drive-train.

As schematically shown in Fig. 1, the rotor transmits mechanical power to the pump that generates a high-pressure flow rate necessary to drive the motor, connected to the electric generator. Both pump and motor are digital-displacement machines. Other components of the hydrostatic transmission are valves, a hydraulic accumulator, filters, oil coolers, a small system necessary to set the minimum pressure in the hydraulic circuit, along with a control unit of the complex system.

Fig. 2 shows a schematic cross-section of a radial piston unit, whose displacement volume can be increased just by adopting more banks in parallel [15]. Two digital solenoid-driven poppet valves, the first arranged along the piston axis and the second
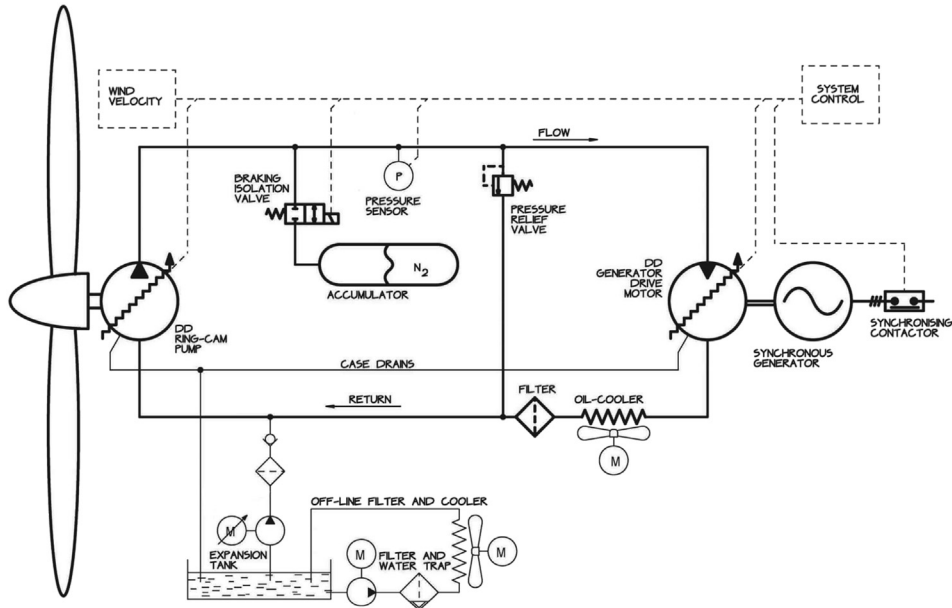
Fig. 1. Schematic of a hydrostatic transmission integrated in a wind energy conversion system.
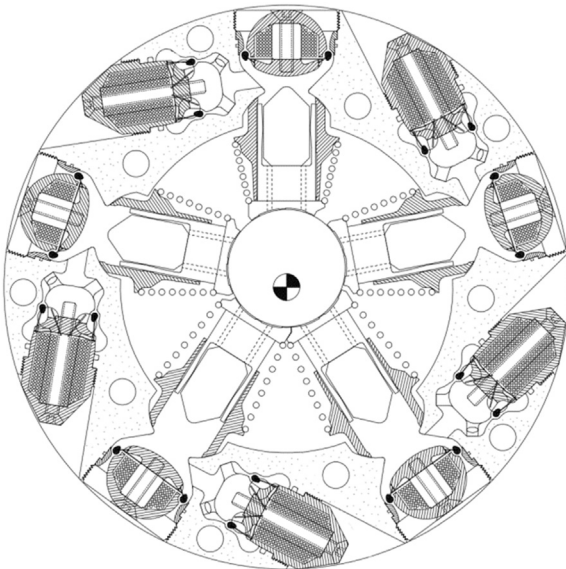

Fig. 2. Cross-section of a digital displacement machine [15].

laterally, control the flow rates entering and exiting each variable volume chamber. Although it is unusual to use a radial eccentric geometry with fast machines, digital valves make this arrangement possible. However, solutions with a two-lobe [20] or a multi-lobe [16] cam ring, rather than an eccentric, are possible as well.

3. Wind turbine drive train modeling

The numerical algorithm implemented to investigate the drive-train performance takes the energy model of each component of the turbine drive-train into account. Once the efficiency of each component has been modeled in terms of performance, it is possible to evaluate the amount of power loss in each component and to calculate the electrical power production for a specific wind

condition. The model used to simulate different turbine drive-train configurations is based on the schematic in Fig. 3, where the ideal power of the wind stream (on the left) is converted into the electrical power output (on the right) through sequential power conversions.

Since the operating conditions of the wind turbine components vary significantly depending on the actual wind speed, a model for each component present in the drive-train was implemented as a function of the variables that affect its performance. Such variables are reported at the top of Fig. 3. As for the bearings and the transformer, the performance only depends on one variable, i.e. angular velocity and power respectively, whereas the performance of the other components is more complex to evaluate, e.g. for the generator at least two variables must be considered.

A delicate task lies in evaluating the performance of the rotor for variable wind speeds, since each turbine has a rotor with specific geometry and characteristics. Moreover, the performance of the rotor depends considerably on the control strategies adopted (pitch angle and rotational speed). In order to solve this problem, a mathematical model was finely tuned to fit the experimental data available from a state-of-the-art 2.0 MW DFIG wind turbine, characterized with a rotor diameter equal to 90 m, present in an Enel wind farm. The experimental data include wind speed, electrical power output, rotational speed and pitch angle over a significant time period, with a 10-min sampling interval. This great deal of data was filtered and processed according to the bin method, as outlined in the IEC (International Electrotechnical Commission) 61400-12-1 international standard [21] and applied in Refs. [22,23], in order (i) to eliminate acquisition errors and (ii) to obtain the power curve of the real turbine along with the rotational speed and pitch angle characterization. The dispersion of the experimental power data for a given wind speed was evaluated by means of the standard deviation that resulted in an average value of 58.7 kW. The most probable reason for such a result is related to the data acquisition system whose averaging method over the 10-min sampling interval could be affected by quick variations of wind speed along with wind blasts. Moreover, the wind speed is measured over the turbine nacelle, so the undisturbed wind speed
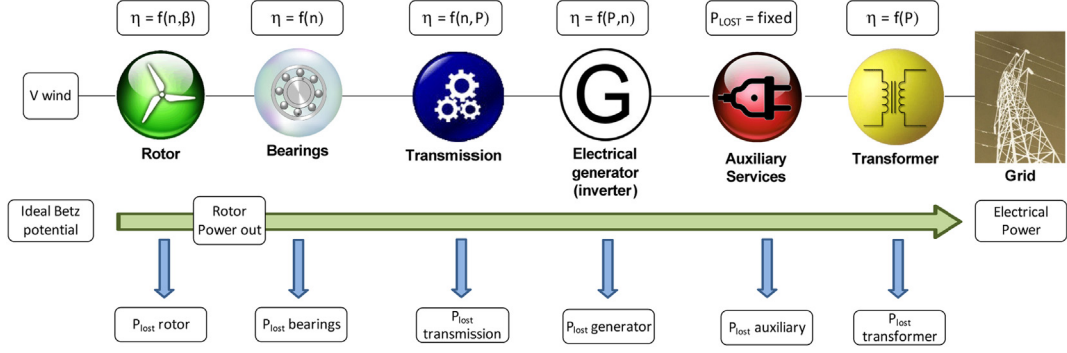
Fig. 3. Drive-train components and power conversions.

calculated by the acquisition system provided by the turbine manufacturer could differ from the real one.

In order to finely tune the mathematical model of the rotor, the mechanical power transmitted from the rotor to the shaft ("Rotor power out" in Fig. 3) was determined for each data point, starting from the electricity production registered by the data logger. Such a task was performed by means of the "inverse" drive-train modeling, which is similar to the "direct" modeling schematized in Fig. 3. In this case, the power loss of each component was added to the electrical power output, allowing for the assessment of the rotor power output.

In the next paragraphs, the model simulating the performance of each component is presented: the model of the rotor is obtained by the inverse drive-train model. Later, the direct drive-train model is validated by a comparison with the experimental data.

3.1. Rotor

The power coefficient of the rotor (Cp) is the ratio between the mechanical power transmitted from the rotor to the shaft and the ideal power that could be exploited from the wind stream. Referring to a specific rotor, such a coefficient depends mainly on both the tip speed ratio (λ) and the pitch angle (β), as shown in Fig. 4 [24]. The tip speed ratio accounts for the velocity at the rotor blade tip divided by the actual velocity of the wind, while the pitch angle is measured between the rotation plane of the rotor and the chord of the wing.

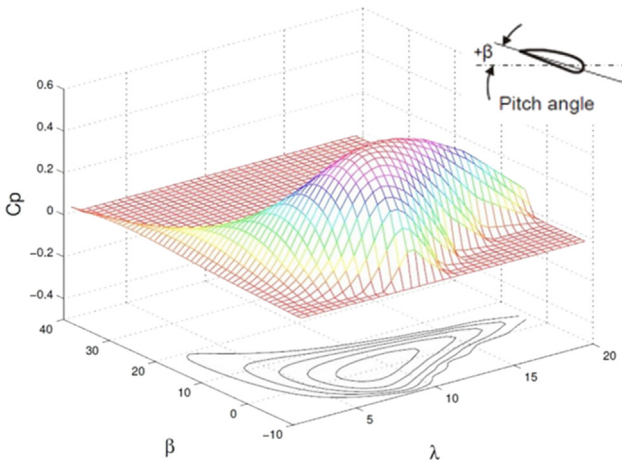In order to evaluate rotor performance for different operating conditions, several mathematical expressions were preliminarily examined in this study [1,2,25]. For each expression, a number of coefficients were adjusted to closely fit the experimental data and the mean square error was calculated. The best fit was obtained with the following equation:

$$Cp = a_1 \cdot \left(\frac{a_2}{\lambda} - a_3 \cdot \beta - a_4 \cdot \beta^{a_5} - a_6 \right) \cdot e^{\frac{a_7}{\tau}} \tag{4}$$

where

$$\tau = \left[\frac{1}{\lambda - a_8 \cdot \beta} - \frac{a_9}{\beta^3 + 1} \right]^{-1} \tag{5}$$

The nine coefficients a_1 to a_9 obtained with a regression for the best fit are detailed in the Appendix.

Fig. 5 shows an appreciable agreement between the equation modeling rotor performance and the experimental data: the pitch angle corresponding to each value of tip speed ratio is assumed to be equal to the experimental one. The maximum efficiency of the rotor is equal to 0.418, evidently less than the ideal limit (0.593) coming from Betz's theory [1,2].

3.2. Gearbox

The model used to simulate the gearbox takes into account variable losses, proportional to the power flow (i.e. friction among the teeth that varies with load), and fixed losses, independent of the power flow. Both losses are evaluated as a function of the number of planetary and parallel stages:

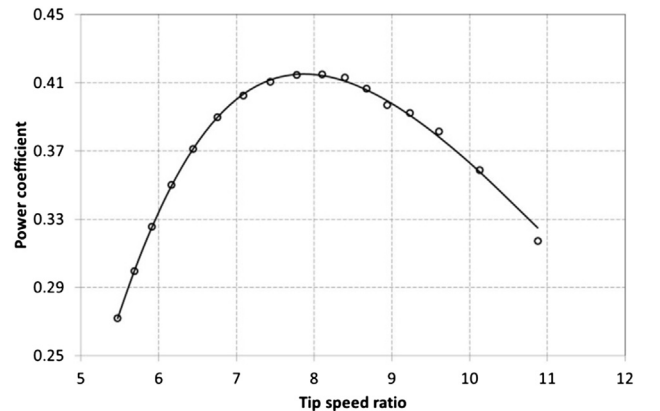$$\Psi_{\text{fixed}} = \Psi_{\text{s+b}} + \Psi_{\text{fl}} \cdot i_{\text{pl+pa}} \tag{6}$$

Fig. 4. Power coefficient as a function of tip speed ratio and pitch angle [24].

Fig. 5. Comparison between Eq. (4) and experimental data (dots).

$$\Psi_{\text{variable}} = \Psi_{\text{o}+\text{b}} + \Psi_{\text{pa}} \cdot i_{\text{pa}} + \Psi_{\text{pl}} \cdot i_{\text{pl}} \tag{7}$$

$$\eta_{\text{gearbox}} = 1 - \left(\Psi_{\text{variable}} + \Psi_{\text{fixed}} \cdot \frac{P_{\text{nom}}}{P} \right) \tag{8}$$

where P_{nom} and P are the nominal and the actual power input to the gearbox, respectively. The values of the five parameters in Eqs. (6) and (7) are reported in the Appendix. Bearing losses are taken into account as well, according to the schematic in Fig. 3.

Referring to a common gearbox layout, with two planetary stages and one parallel stage, the efficiency resulting from Eq. (8) is close to 0.96, for power input greater than 50% of the nominal power, and decreases rapidly for power input less than 20%.

3.3. Electrical generator and inverter

The combination of mechanical, electrical and magnetic phenomena occurring inside the generator brings about different losses that are anything but easy to be evaluated. In particular, the model for evaluating losses in DFIG, PMG and SCIG (squirrel cage induction generator) units reported in Ref. [26] was implemented in this work, along with a model of the rotor inverter associated to the DFIG unit and the full-scale converter associated to both PMG and SCIG.

Power input and rotational speed are the main variables that affect the performance of generator and inverter: the maximum efficiency for both components is obtained with a power input close to the nominal value and a rotational speed ranging from the nominal to the maximum value.

Several losses occurring in a generator were considered and modeled: mechanical losses, core losses (hysteresis and eddy currents), stator and rotor Joule losses, rotor windage losses (due to the presence of air in the gaps between rotor and stator). On the other hand, the model of the inverter considers conduction losses, switch losses, diode conduction losses, diode switch losses and filter losses.

Both power input and rotational speed were varied over a wide range, so efficiency maps for generator and inverter were calculated. The combination of such maps returns the overall efficiency of the generator–inverter system, as reported in Fig. 6 for a DFIG unit. The parameters used to calculate the performance of the generator–inverter system are reported in the Appendix.

3.4. Auxiliary systems

There are several auxiliary systems in a modern wind turbine and the related power consumption could be significant in off-peak conditions. They are generally powered at low-voltage and located
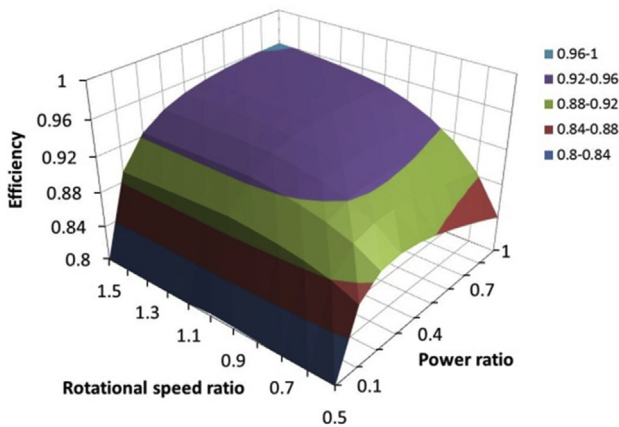

Fig. 6. Overall performance of DFIG and inverter as a function of rotational speed and power input.

between the generator and the transformer, as schematized in Fig. 3. The most important auxiliary systems are dedicated to (i) cooling, (ii) yaw and (iii) pitch control.

Cooling system power consumption could be as high as 1–1.5% of the nominal power of the wind turbine. A linear relation to the electrical power output of the turbine is generally accepted. In this study, thanks to the availability of additional technical data reported in the technical datasheet of the machine, such a power demand has been included partly in the generator and partly in the gearbox model. As regards yaw and pitch control systems, which are activated in an intermittent mode, their average power consumption is generally much lower than the nominal one, here considered in the range of 0.2–0.3% of the turbine nominal power.

3.5. Transformer

Power losses at the transformer are mainly due to Joule and hysteresis effect and induction in the metal support structure. The first two losses depend on power input, while the third is almost load-independent. Transformer efficiency was calculated as a function of the power input [2]:

$$\eta_{\text{tr}} = 1 - \left[\frac{1}{3} \cdot (1 - \eta_{\text{nom}}) \cdot \frac{P_{\text{nom}}}{P} + \frac{2}{3} \cdot (1 - \eta_{\text{nom}}) \right] \tag{9}$$

where P is the instantaneous power input to the transformer, and P_{nom} is the nominal power. In particular, η_{nom} was fixed equal to 0.99 for all the investigated drive-train configurations.

3.6. Hydrostatic transmission

Pump and motor are the main components of the hydrostatic transmission.

The pump is driven by the rotor at a speed equal to n_{p} and generates a flow rate that is known to be less than the product of the measured machine displacement volume and the number of revolutions per unit of time [19]. Introducing the volumetric efficiency, it is possible to estimate such a volumetric flow rate:

$$Q_{\text{p}} = \eta_{\text{v,p}} \cdot \alpha_{\text{p}} \cdot V_{\text{p}} \cdot n_{\text{p}} \tag{10}$$

A thorough model of the volumetric efficiency is proposed in Ref. [27]: leakages and fluid compressibility are responsible for the main volumetric losses.

Once the theoretical flow rate is calculated according to the number of pumping elements:

$$Q_{\text{p,th}} = z_{\text{p}} \cdot V_{1,\text{p}} \cdot n_{\text{p}} \tag{11}$$

and the volumetric efficiency is re-written to highlight fluid losses:

$$\eta_{\text{v,p}} = \frac{Q_{\text{p,th}} - Q_{\text{p,l}}}{Q_{\text{p,th}}} \tag{12}$$

the following final equation is considered to account for fluid losses in a digital-displacement pump:

$$\eta_{\text{v,p}} = 1 - \Psi_{\text{L,p}} \cdot \frac{\Delta p_{\text{p}}}{\mu \cdot n_{\text{p}}} - (1 + \xi_{\text{p}}) \cdot \frac{\Delta p_{\text{p}}}{B} \tag{13}$$

The parameter α_{p} that determines the current displacement volume of the pump is not present in Eq. (13), so that a digital-displacement pump has the same volumetric efficiency despite the number of elements that actually pump during a working cycle. As a matter of fact, if the suction valve of a pumping chamber is open throughout the working cycle, there is no significant pressure

drop between the suction volume and the chamber and, consequently, leakage and fluid compressibility are really negligible and not comparable to the tens of MPa as pressure difference between outlet and inlet of the pump. Different considerations concern the pumping elements of a state-of-the-art positive-displacement pump, e.g. a swash-plate-type piston unit with port plate [28], where all the pistons work, even at intermediate displacement, just reducing the stroke of each piston.

Eq. (13) proposed for the pump can be revised for the motor. In this case, the volumetric efficiency is similarly determined as:

$$\eta_{v,m} = \frac{Q_{m,th}}{Q_{m,th} + Q_{m,l}} = \frac{1}{1 + \Psi_{L,m} \cdot \frac{\Delta p_m}{\mu \cdot n_m} + (1 + \xi_m) \cdot \frac{\Delta p_m}{B}} \quad (14)$$

On the other hand, a model considering only volumetric losses is not sufficient: hydraulic-mechanical losses in both the pump and the motor must be taken into account.

The actual torque required by the pump is calculated as

$$T_p = \frac{\alpha_p \cdot V_p \cdot \Delta p_p}{\eta_{hm,p}} \quad (15)$$

and differs from the theoretical one just for the presence of the hydraulic-mechanical efficiency at the denominator. Similarly, the output torque at the motor shaft is calculated as

$$T_m = \eta_{hm,m} \cdot \alpha_m \cdot V_m \cdot \Delta p_m \quad (16)$$

Torque losses in hydrostatic units are mainly due to friction forces in lubricated gaps present inside the machine elements in relative motion [29]. Dealing with a hydraulic motor, they must be deducted from the theoretical output torque:

$$T_m = T_{m,th} - T_{m,l} = \alpha_m \cdot V_m \cdot \Delta p_m - T_{m,l} \quad (17)$$

In particular, the torque loss is the sum of:

- the friction torque, which is proportional to the load, i.e. to the pressure difference between inlet and outlet of the motor, by means of a friction coefficient that is maximum when the rotational speed is zero and decreases as speed increases;
- the viscous friction torque, which is proportional to fluid viscosity, rotational speed and characteristic dimensions of the machine that can be similarly quantified as proportional to the displacement volume of the machine;
- the constant friction torque, independent of operating conditions.

No turbulent friction component is here considered for the sake of simplicity.

Thus, the hydraulic-mechanical efficiency of the motor is formulated as:

$$\eta_{hm,m} = 1 - \Psi_{f,m} \cdot \frac{1}{\alpha_m \cdot n_m} - \Psi_{vf,m} \cdot \frac{\mu \cdot n_m}{\alpha_m \cdot \Delta p_m} - \Psi_{k,m} \cdot \frac{1}{\alpha_m \cdot \Delta p_m} \quad (18)$$

Similarly, the hydraulic-mechanical efficiency of the pump is:

$$\eta_{hm,p} = \frac{1}{1 + \Psi_{f,p} \cdot \frac{1}{\alpha_p \cdot n_p} + \Psi_{vf,p} \cdot \frac{\mu \cdot n_p}{\alpha_p \cdot \Delta p_p} + \Psi_{k,p} \cdot \frac{1}{\alpha_p \cdot \Delta p_p}} \quad (19)$$

Looking at the equations returning both volumetric and hydraulic-mechanical efficiencies, it is possible to realize that intermediate displacement volumes affect only the latter. As a matter of fact, if partial displacement mode does not affect volumetric losses as previously highlighted, piston motion inside the cylinder is always subject to friction, resulting in a torque loss.
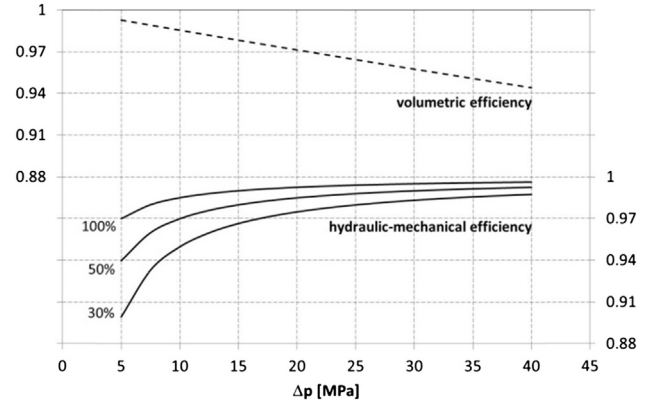
Fig. 7. Volumetric and hydraulic-mechanical efficiencies of the simulated digital-displacement motor rotating at 1500 rpm (in dashed and continuous lines, respectively).

Referring to the volumetric and hydraulic-mechanical efficiencies for both pump and motor, and neglecting pressure drops in the lines connecting the two digital-displacement units, it is possible to model the efficiency of the hydrostatic transmission by setting the coefficients present in the equations above. These coefficients are detailed in the Appendix, and were determined in order to fit the results of the digital-displacement unit investigated in Ref. [30], once fixed fluid properties in terms of bulk modulus (1400 MPa) and viscosity (32 cP).

As an example, according to Eqs. (14) and (18), Fig. 7 shows both volumetric and hydraulic-mechanical efficiency depending on the pressure difference between inlet and outlet of the motor rotating at 1500 rpm. Three normalized values of displacement volume are reported, showing that efficiency values remain high even at lower loads and displacement volumes.

Finally, both pump and motor models were integrated and used to assess the overall efficiency of an advanced hydrostatic transmission with one pump, directly driven by the rotor, delivering high-pressure fluid to two motors in a parallel configuration, driving two separate generators. Thus, for each input to the system in terms of power and rotor speed, a routine was created in order to calculate the displacement volumes of the machines and the maximum pressure of the hydraulic circuit determining the maximum efficiency of the system. The result of such a control procedure is the overall efficiency of the hydrostatic transmission, as shown in Fig. 8. In particular, it can be seen that only one motor is used when input power is less than 16% of the nominal power, whereas both motors run for higher inputs, with an overall
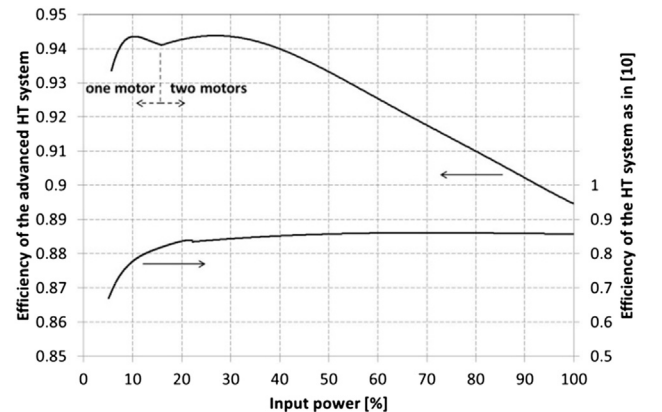
Fig. 8. Efficiency comparison for the advanced hydrostatic transmission and the conventional HT system as in Ref. [10].
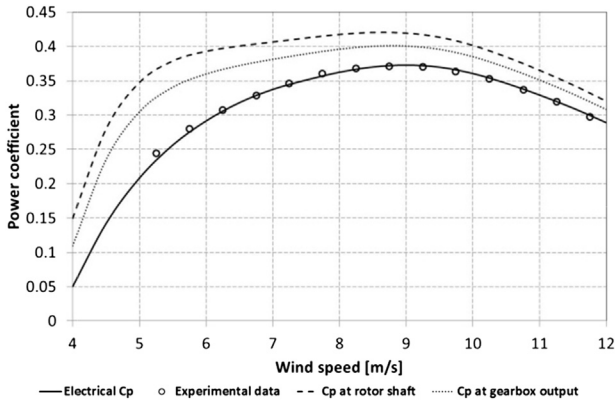
Fig. 9. Power coefficients and comparison with experimental data.

efficiency sensibly higher than the one of the system adopted in Ref. [10], where state-of-the-art positive-displacement units were used.

4. Model validation

In order to test the accuracy of the drive-train model, the performance of the turbine whose experimental data were available was simulated. Experimental pitch angle and tip speed ratio were used for each wind speed.

Referring to Fig. 9, power coefficients calculated with the numerical model are presented with lines, while dots represent the experimental data, obtained with the bin method, as previously described. The graph shows a good correspondence between the calculated electrical and experimental power coefficients. The Cp curves calculated at rotor and gearbox output (see Fig. 3) are reported as well, even though no data are available for a comparison. The difference between the Betz's value and the ones returned by the dashed line (rotor output) is related to aerodynamic losses of the rotor and to downstream kinetic energy. The difference between the dashed and the dotted lines (gearbox output) is related to mechanical losses of bearings and gearbox, while the difference between the dotted and the continuous lines (transformer output) is related to the losses of generator–inverter, auxiliary systems and transformer. The difference between rotor output and transformer

output at low wind speeds results in a quick drop of the second curve, while the first one presents an almost flat slope for wind speeds below 9 m/s. The lower efficiency of gearbox and electric generator at partial loads is responsible for such a behavior.

The annual energy production calculated by the model in comparison with the measured values is a further evaluation of the model accuracy. The experimental wind speed distribution, as reported with vertical bars in Fig. A1 in the Appendix, was used: it can be represented by a Weibull distribution whose shape and scale parameters are equal to 1.9 and 6.8 respectively. The same availability (0.968) of the real turbine was used. The annual energy production as predicted by the model is 4199 MWh vs. 4271 MWh as a measured value. Considering that the difference is less than 2%, the simulation model can be considered sufficiently reliable.

However, since the availability of the advanced hydrostatic transmission is not known to the author's knowledge, as regards the next comparison of different drive-train configurations, an availability factor equal to 1 is used for all the drive-train configurations in the following. According to such a hypothesis, the annual energy production of the real turbine would be equal to 4338 MWh.

5. Drive-train configurations and simulation criteria

A set of drive-train configurations was investigated in order to obtain benchmark values useful for discussing the performance of a drive-train with the advanced hydrostatic transmission. Referring to each drive-train configuration with the same rotor, i.e. the one of the real machine, and adopting the measured annual wind speed distribution, simulations were run to obtain power coefficient and power curves and to calculate the annual energy production.

5.1. Drive-train with DFIG unit

The first drive-train configuration (Fig. 10a) reproduces the real turbine (referred to as C1 in the following), whose power coefficient curves are detailed in Fig. 9. A three-stage gearbox with a gear ratio of 104:1 is present between rotor and generator. The DFIG unit is connected to the rotor inverter, which controls the speed of the magnetic field around the rotor, with about one-third of the total power output that turns back to the generator. A maximum rotor speed ratio (n_{max}/n_{min}) equal to 1.35 is possible with this
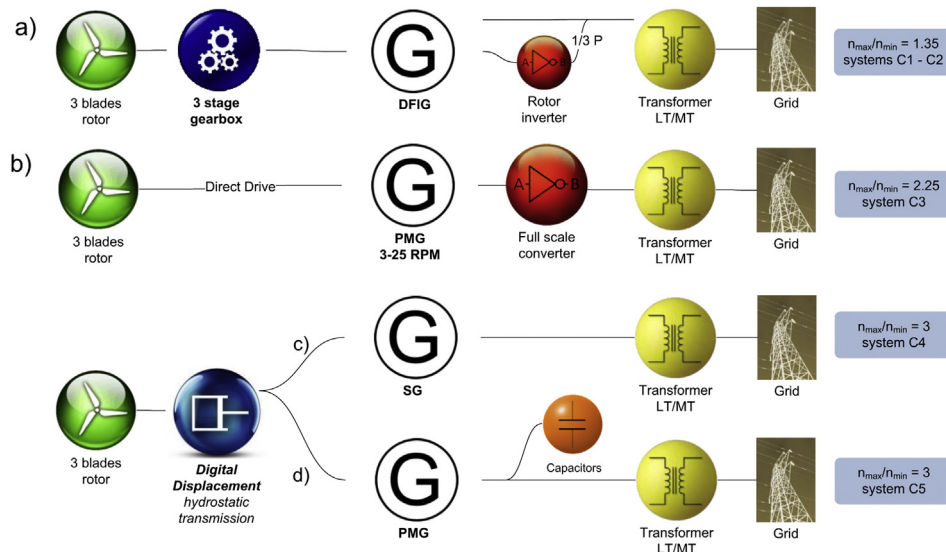

Fig. 10. Investigated drive-train configurations: schematic a) is representative of systems C1 and C2; schematic b) is representative of systems C3; schematics c) and d) are representative of systems C4 and C5 respectively.

configuration, due to the limitation of the generator itself, so the wind speed interval where the tip speed ratio is constant is reduced. The main advantage of this configuration consists in the small size of the inverter: a low amount of energy is converted with reduced energy losses. On the other hand, a frequent maintenance is required to change the slip rings used to power up the rotor and the reactive power supplied by the turbine can be controlled within a limited range (generally $\cos \varphi = 0.96-0.98$). Until a few years ago this drive-train configuration was the most flexible and efficient among the commercially available solutions: as a consequence, a large number of such turbines has been installed. The drive-train configuration schematized in Fig. 10a is also adopted for the system C2, as detailed in the following.

5.2. Drive-train with direct-drive PMG unit

According to the direct-drive configuration presented in Fig. 10b (in the following as system C3), the rotor is directly connected to the generator with no gearbox. A large diameter and multi-pole generator is necessary to provide the required torque. This type of generator is usually made with permanent magnets in order to eliminate the Joule losses present in the rotor of an excited generator, due to the very high currents required for a high resistant torque. Such a drive-train configuration allows a high rotor speed ratio (about 2.25, as deduced from technical datasheets of several commercial turbines) with a high average efficiency of the rotor. The full scale converter allows to regulate the power factor of the turbine over a wide range, and to control the output voltage. The main source of breakdown is also eliminated, along with the losses related to the gearbox. On the other hand, a large-size converter is required and all the power generated is affected by the inverter losses. This component requires a periodic maintenance and needs a replacement after several years, even though this problem is mitigated by the progressive inverter cost reductions of the last decade.

5.3. Drive-trains with the advanced hydrostatic transmission

Two schematic drive-train configurations with an advanced hydrostatic transmission are presented in Fig. 10c and d. As compared to system C1, the gearbox is replaced by the hydrostatic transmission and no inverter is present, since the generator runs at constant speed. The control of the displacement volumes of both pump and motor allows to obtain a rotor speed ratio as high as necessary. As previously highlighted, the main advantages of such a configuration are (i) the limitless range of the rotor speed, (ii) the potentially high reliability and low maintenance requirements of the hydrostatic drive, against a conventional gearbox, and (iii) the possibility to reduce the weight of the nacelle. On the other hand, a reduction of the nominal Cp value is expected, as a consequence of the lower overall efficiency of the hydrostatic transmission (see Fig. 8).

The best performance of the hydrostatic transmission, in terms of turbine cost and Cp curve, can be achieved by means of a fast generator, typically running at 1500 rpm. In order to allow a reactive power regulation (with typical $\cos \varphi$ in the range from 0.8 to 1), a synchronous and externally excited generator can be used: this configuration is referred to as C4. However, due to the presence of slip rings, this solution reduces the reliability of the drive-train, which is one of the most interesting potential advantages of the hydrostatic transmission. Moreover, the efficiency of this generator at partial loads decreases, owing to Joule losses in the rotor, whose current must be high to achieve the desired resistant torque. Thus, two configurations with hydrostatic transmission were simulated: the first (Fig. 10c) includes the above-mentioned synchronous generator, while the second (Fig. 10d) uses a fast PMG unit, referred to as C5. The latter has a high efficiency over all the working range, a

high reliability and requires few maintenance. On the other hand, it does not allow a reactive power control and requires a bank of capacitors to compensate the inductive power generation.

As detailed in Fig. 10, the rotor speed ratio n_{max}/n_{min} possible with the hydrostatic transmission has been set equal to 3, which allows to guarantee constant tip speed ratio, reflecting on a maximum efficiency of the rotor, for wind speeds lower than the nominal value.

5.4. Simulation criteria

Pitch angle and rotational speed are adjusted by the control system of the turbine as a function of wind speed. They are the most important parameters affecting rotor performance and have to be controlled with specific strategies.

Fig. 11 shows a typical power curve of a wind turbine. If wind speed is less than v_{cut-in}, it is neither possible nor convenient to run the turbine. When wind speed increases, up to $v_{\omega N}$, the electrical power production has to be maximized by means of a pitch angle and a tip speed ratio close to the optimum values. The rotational speed is constant and equal to its maximum value for wind speeds ranging from v_{rated} and $v_{cut-off}$, while the pitch angle is varied in order to limit the power to its nominal value. Fig. 11 also shows an interval of wind speeds, between $v_{\omega N}$ and v_{rated}, where the pitch angle is varied to achieve a progressive transition from the two contiguous regions. Finally, when wind speed is greater than $v_{cut-out}$, rotor blades would be subject to overloads, so the turbine is stopped to avoid damages.

In order to allow a consistent comparison of the different drive-train configurations reported in Fig. 10, fixed control strategies were considered for wind speeds ranging from v_{cut-in} to $v_{\omega N}$ (as detailed in Fig. 11):

- rotor speed variation oriented to maintain the tip speed ratio constant over an as wide as possible range, according to the speed limitations imposed by the generator;
- pitch angle variation in order to achieve the maximum efficiency of the rotor, in case of generator speed limitations.

Moreover, the following parameters were determined:

- v_{cut-in} corresponding to an electrical power output equal to 1.5% of the nominal power;
- v_{rated} corresponding to an electric power output equal to the nominal value, i.e. 2.0 MW.

Since the control strategies of the real turbine do not always match these three modes, a simulation of a DFIG turbine (referred to as C2), here revised to comply with the above-mentioned specifications, was run. An annual energy production 4% higher than the experimental one and a Cp curve closer to the one declared by the manufacturer were achieved.
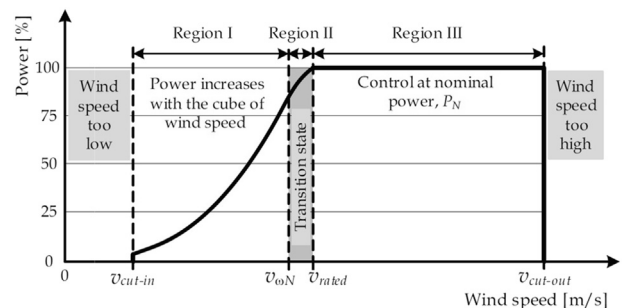
Fig. 11. Schematic of the regions for a pitch- and speed-controlled multi-MW wind turbine [31].

A comparison between the control strategies of systems C2 and C5 is presented in Fig. 12. One can see that the wider range for rotor speed variation of system C5, which is equal to 3, brings about an extension of the constant tip speed ratio region, which covers all the range from $v_{\text{cut-in}}$ to $v_{\omega N}$, with respect to the case of system C2. As a consequence, system C5 presents lower values for $v_{\text{cut-in}}$ and $v_{\omega N}$ and an earlier achievement of the nominal power due to the tip speed ratio closer to the optimal value. Moreover, the pitch angle is constant over the region where the tip speed ratio is constant in system C5, due to hydraulic similitude, and the rotational speed varies linearly with the wind speed. When wind speeds exceed $v_{\omega N}$, higher pitch angle variations are required in system C5 than in system C2 to balance the rotor efficiency.

6. Results

One of the most significant results of the simulation consists of the power coefficient that indicates the performance of the turbine over its functioning region. It synthesizes the behavior of the several systems present in the drive-train, taking control strategies into account.

Looking at Fig. 13, system C1 is the most penalized owing to the lower range for rotor speed variation, with the exception of wind speed greater than the nominal value when similar behaviors can be appreciated for all the systems. The curve of system C2 returns values that are slightly higher than the ones for system C1, just for the modified control strategy. System C4 presents higher performance, thanks to its wider rotational speed range: the power coefficient is almost constant from 7 to 11 m/s and equal to its maximum value. However, when wind speed reduces, the synchronous generator, operating at partial load, seriously affects overall performance, which is even higher than the ones of systems C1 and C2. When wind speed is lower than 7 m/s, the better performance of the PMG unit at partial load makes system C5 preferable to system C4, even though small differences between the two configurations can be appreciated for higher wind speeds, since the synchronous generator is more efficient at nominal load. On the other hand, system C5 can result critical from a grid regulation point of view, since neither reactive power nor output voltage controls are possible. Ultimately, the highest power coefficients characterize system C3, thanks to (i) no gearbox, (ii) wider range of rotor speed variation and (iii) the high efficiency of the PMG unit with the full scale converter. However, there is a narrow interval where lower rotational speeds cannot be efficiently processed by the inverter.

Compared to systems C1 and C2, an optimum tip speed ratio even at high wind speeds allows systems C3, C4 and C5 to supply the nominal power at lower wind speeds. In particular, this is a
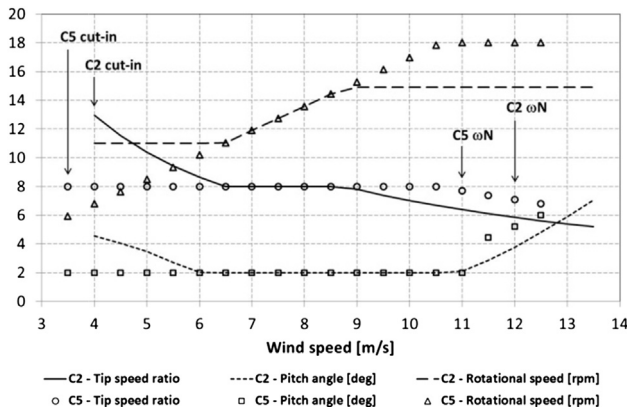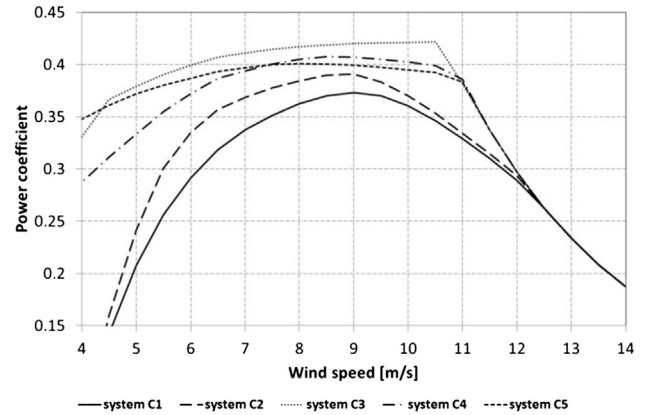
Fig. 13. Power coefficients of the different drive-train configurations.

feature of system C3, as highlighted with a sharp discontinuity in the curve in Fig. 13.

Thanks to the numerical model, it is possible to detail the overall power balance of the drive-train for each specific wind speed. With particular reference to the annual energy production of system C1, a detailed balance of net energy to the grid, energy losses in the drive-train components and energy consumptions by auxiliary systems is reported in Fig. 14, where the sum of all the slice contributions returns the ideal energy production according to Betz. Such a production was calculated assuming the ideal power output predicted by Betz for wind speeds ranging from $v_{\text{cut-in}}$ to $v_{\omega N}$ and the measured wind distribution. Since for wind speeds greater than $v_{\omega N}$ an energy dissipation occurs, the analysis detailed in Fig. 14 is limited to the Region I of Fig. 11. In detail, the pie-graph in Fig. 14 represents a "second-law" analysis of the drive-train with an efficiency equal to 55.1%. The aerodynamic behavior of the rotor is responsible for the main losses, which are split into two slices. The first (RL1) is related to the specific blade geometry and accounts for fluid-dynamic losses present even if the optimum pitch angle and tip speed ratio are set for each wind speed. The second (RL2) always accounts for fluid-dynamic losses, but is due to limitations imposed by pitch angle and tip speed ratio control.

Results similar to the ones reported in Fig. 14 can be presented also for the other drive-train configurations. In order to reduce the amount of results subject to comparison, reference to Fig. 15 is made, where the losses of each system are grouped by type. Moving from the left to the right, losses related to rotor geometry do not vary (the rotor is the same in all the systems), but losses due to non-optimum pitch angle and tip speed ratio control are significantly
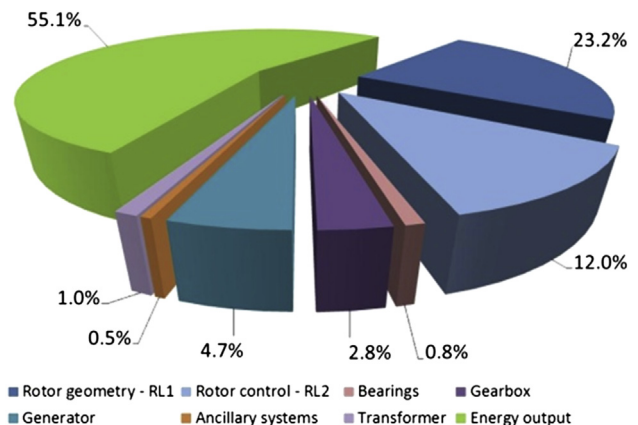
Fig. 12. Control strategies adopted for the simulation of systems C2 and C5.

Fig. 14. Overall annual energy balance for system C1 (each contribution is related to Betz's theoretical power output).
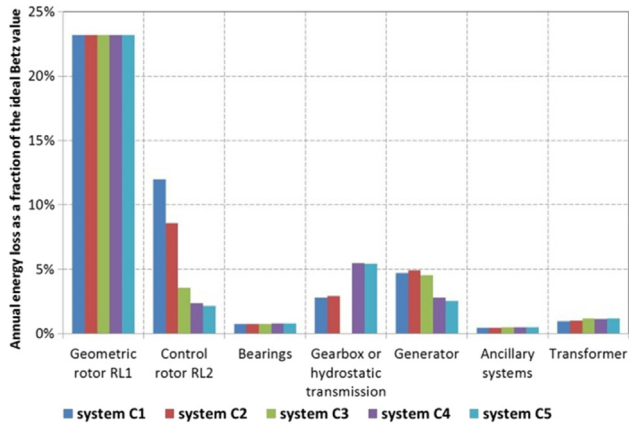
Fig. 15. Comparison of annual energy losses characteristic of the investigated drive-trains.

Table 1
Calculated annual energy productions.

System	Energy production [MWh/year]	Variation
C1: current drive-train with DFIG unit	4338	−4%
C2: optimized drive-train with DFIG unit	4520	−
C3: drive-train with direct-drive PMG unit	5045	11.6%
C4: drive-train with HT and SG unit	4895	8.3%
C5: drive-train with HT and PMG unit	4920	8.8%

reduced in systems C3 to C5. System C3 has neither gearbox nor hydrostatic transmission, whose losses are almost twice the gearbox losses in systems C1 and C2. As regards the losses at the electric generator, higher values characterize systems C1 to C3, due to the presence of the inverter. Losses at bearings, auxiliary systems and transformer are almost equal for each system.

The data reported in Fig. 15 are based on the measured wind speed density distribution. As for lower scale parameters (narrow distribution curves), simulations also showed that RL2 losses of systems C1 to C3 are reduced if the drive-train configuration is adjusted in order to match the optimum working point with the most frequent wind speed.

Finally, annual energy productions of the five investigated systems are reported in Table 1. Considering system C2 as a reference, systems C4 and C5 seem to be interesting at a glance, since energy production increases. Moreover, the drive-train with the hydrostatic transmission should be more reliable than the DFIG one, since both gearbox and slip rings are eliminated. Nevertheless, Table 1 highlights the superiority of system C3, which seems to be the preferable solution from an energy production point of view, even

though issues related to component cost and reliability should be considered in order to choose the best configuration for the wind energy conversion system.

7. Conclusions

Starting from design and experimental data available for a state-of-the-art 2 MW DFIG wind turbine, a numerical model was implemented to investigate the performance of wind energy conversion systems with drive-train configurations different from the original one.

The first analysis focusing on the original system highlighted the importance of a proper control system, oriented to increase the annual energy production. In fact, experimental data showed a non-optimized control of the examined wind turbine, so an increase in annual energy production seems to be possible through an improvement of the rotor control strategy.

A direct-drive layout was considered as well, and the most favorable energy production was calculated. The absence of components, in contrast with the original configuration, should increase system reliability, being the inverter the only cause of fault in this case. However, full voltage, frequency and reactive power controls are not feasible without an FSC (full scale converter) unit.

The use of an advanced hydrostatic transmission in the drive-train was finally studied, as the scope of the work. Compared to the direct-drive layout, from an energetic point of view, this solution could be interesting when the wind speed is near the cut-in value. On the other hand, reductions of the hydrostatic transmission efficiency occurring at higher wind speeds, significantly penalize the performance of the whole drive-train. Regarding the generator, two different solutions were considered: with a PMG unit it is possible to reach great reliability as well as high part load efficiency, whereas with a synchronous generator the reactive power output can be adjusted. Both evaluated hydrostatic configurations return about 8–9% more in terms of yearly electricity production with respect to a DFIG turbine and approximately 3% less compared to a direct-drive PMG configuration. In any case, a hydrostatic transmission could be useful to (i) lower the drive-train cost, (ii) improve system reliability and (iii) reduce the weight of the nacelle. The last two features could be key points for off-shore applications, although the higher average wind speed in open sea could increase the energy balance difference with respect to the PMG system, due to the lower efficiency of the hydrostatic transmission at full load. Further evaluations concerning costs, as well as considerations about the scenario in which the wind farm will be operated, should drive the choice of the proper drive-train layout.
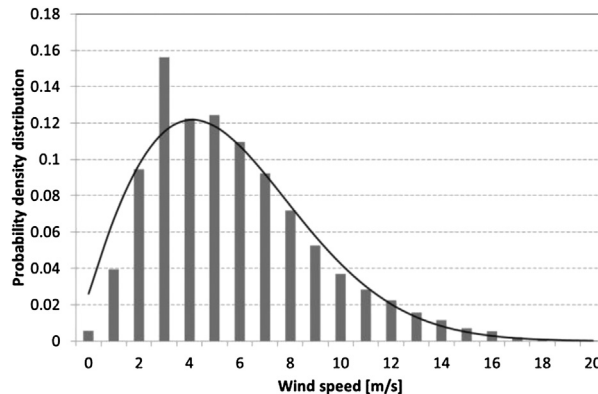
Appendix

Fig. A1. Density distribution of the measured wind speed (bars indicate the wind speed distribution, along with the Weibull curve with shape and scale parameters equal to 1.9 and 6.8 respectively).

Table A1
Best fit coefficients in Eqs. (4) and (5).

a_1	1.53
a_2	67.87
a_3	−0.09
a_4	0
a_5	4.90
a_6	5.09
a_7	20.21
a_8	−0.02
a_9	0

Table A2
Coefficients in Eqs. (6) and (7).

Ψ_{s+b}	$2 \cdot 10^{-3}$
Ψ_{fl}	$1 \cdot 10^{-3}$
Ψ_{o+b}	$1.8 \cdot 10^{-3}$
Ψ_{pa}	$1.1 \cdot 10^{-2}$
Ψ_{pl}	$8 \cdot 10^{-3}$

Table A3
Coefficients of the DFIG model [26].

Generator nominal speed [rpm]	1620
Line out voltage [V]	690
Rotor resistance [Ω]	$3.65 \cdot 10^{-3}$
Stator resistance [Ω]	$1.35 \cdot 10^{-2}$
Iron resistance [Ω]	$6.2 \cdot 10^{-2}$
Magnetic reactance [Ω]	1.776
Rotor/stator windage ratio	3
Windage loss factor [kW/rpm]	$1 \cdot 10^{-3}$

Table A4
Coefficients of the rotor inverter model [26].

DC bus voltage [V]	1100
Switching frequency [Hz]	3000
IGBT fixed portion VCE [V]	1.5
IGBT dynamic resistance [Ω]	$1.36 \cdot 10^{-3}$
Diode fixed portion [V]	1.25
Diode dynamic resistance [Ω]	$5 \cdot 10^{-4}$
IGBT turn-on energy loss [J]	0.45
IGBT turn-off energy loss [J]	0.60
Current for on−off switching [A]	1200
Voltage for on−off switching [V]	900
Diode recovery energy loss [J]	$3 \cdot 10^{-2}$
Fixed loss per bridge [kW]	2
Grid RMS line−line voltage [V]	690
Modulation index [V_{AC}/V_{DC}]	0.887

Table A5
Coefficients in Eqs. (13), (14), (18) and (19).

Coefficient	Pump	Motor
ξ	0.55	0.55
Ψ_L	$1.47 \cdot 10^{-3}$	$1.81 \cdot 10^{-3}$
Ψ_f	$8.75 \cdot 10^{-2}$	$7.39 \cdot 10^{-2}$
Ψ_{vf}	$2.52 \cdot 10^{-2}$	$2.33 \cdot 10^{-3}$
Ψ_k	0.118	0.391

References

[1] Burton T, Sharpe D, Jenkins N, Bossanyi E. Wind energy handbook. John Wiley & Sons; 2001.

[2] Ackermann T. Wind power in power systems. John Wiley & Sons; 2005.

[3] Ribrant J, Bertling ML. Survey of failures in wind power systems with focus on Swedish wind power plants during 1997−2005. IEEE Trans Energy Convers 2007;22(1):167−73. http://dx.doi.org/10.1109/TEC.2006.889614.

[4] Sun X, Huang D, Wu G. The current state of offshore wind energy technology development. Energy 2012;41:298−312. http://dx.doi.org/10.1016/j.energy.2012.02.054.

[5] Ficarella A, Giuffrida A, Lanzafame R. Common rail injector modified to achieve a modulation of the injection rate. Int J Automot Technol 2005;6(4):305−14.

[6] Giuffrida A, Laforgia D. Modelling and simulation of a hydraulic breaker. Int J Fluid Power 2005;6(2):47−56.

[7] Filipi Z, Louca L, Daran B, Lin CC, Yildir U, Wu B, et al. Combined optimisation of design and power management of the hydraulic hybrid propulsion system for the 6 × 6 medium truck. Int J Heavy Vehicle Syst 2004;11(3−4):372−402. http://dx.doi.org/10.1504/IJHVS.2004.005458.

[8] Giuffrida A, Lanzafame R. On the pressure relief valve for the lubrication system of an internal combustion engine. In: Proceedings of the 2007 fall technical conference of the ASME internal combustion engine division, October 14−17, 2007, Charleston, South Carolina, USA. http://dx.doi.org/10.1115/ICEF2007-1716.

[9] Tiţa I, Călăraşu D. Wind power systems with hydrostatic transmission for clean energy. Environ Eng Manag J 2009;8(2):327−34.

[10] Schmitz J, Vatheuer N, Murrenhoff H. Development of a hydrostatic transmission for wind turbines. In: Proceedings of 7th international fluid power conference, March 22−24, 2010, Aachen, Germany.

[11] Browning JR, Manwell JF, McGowan JG. A techno-economic analysis of a proposed 1.5 MW wind turbine with a hydrostatic drive train. Wind Eng 2009;33(6):571−85. http://dx.doi.org/10.1260/0309-524X.33.6.571.

[12] Linjama M. Digital fluid power − state of the art. In: Proceedings of the 12th Scandinavian international conference on fluid power, May 18−20, 2011, Tampere, Finland.

[13] Scheidl R, Linjama M, Schmidt S. Is the future of fluid power digital? Proc Inst Mech Eng Part I J Syst Control Eng 2012;226(6):721−3. http://dx.doi.org/10.1177/0959651811435628.

[14] Ehsan M, Rampen W, Salter S. Modeling of digital-displacement pump-motors and their application as hydraulic drives for nonuniform loads. ASME J Dyn Syst Meas Control 2000;122(1):210−5. http://dx.doi.org/10.1115/1.482444.

[15] Salter SH, Taylor JRM, Caldwell NJ. Power conversion mechanisms for wave energy. Proc Inst Mech Eng Part M J Eng Marit Environ 2002;216(1):1−27. http://dx.doi.org/10.1243/147509002320382103.

[16] Payne GS, Kiprakis AE, Ehsan M, Rampen WHS, Chick JP, Wallace AR. Efficiency and dynamic performance of Digital Displacement™ hydraulic transmission in tidal current energy converters. Proc Inst Mech Eng Part A J Power Energy 2007;221(2):207−18. http://dx.doi.org/10.1243/09576509JPE298.

[17] Manring ND, Luecke G. Modeling and designing a hydrostatic transmission with a fixed displacement motor. ASME J Dyn Syst Meas Control 1998;120(1):45−9. http://dx.doi.org/10.1115/1.2801320.

[18] Kugi A, Schlacher K, Aitzetmüller H, Hirmann G. Modelling and simulation of a hydrostatic transmission with variable-displacement pump. Math Comput Simul 2000;53(4−6):409−14. http://dx.doi.org/10.1016/S0378-4754(00)00234-2.

[19] Ivantysyn J, Ivantysynova M. Hydrostatic pumps and motors. Academia Books International; 2000.

[20] Giuffrida A, Lanzafame R. Cam shape and theoretical flow rate in balanced vane pumps. Mech Mach Theory 2005;40(3):353−69. http://dx.doi.org/10.1016/j.mechmachtheory.2004.07.008.

[21] IEC. Wind turbines − part 12-1: power performance measurements of electricity producing wind turbines. IEC 61400-12-1 international standard; 2005.

[22] Llombart A, Watson SJ, Llombart D, Fandos JM. Power curve characterization I: improving the bin method. In: International conference on renewable energies and power quality, March 16−18, 2005, Zaragoza, Spain.

[23] Llombart A, Watson SJ, Fandos JM, Llombart D. Power curve characterization II: modelling using polynomial regression. In: International conference on renewable energies and power quality, March 16−18, 2005, Zaragoza, Spain.

[24] Kulka A. Pitch and torque control of variable speed wind turbines. MSc Thesis. Göteborg, Sweden: Chalmers University of Technology; 2004.

[25] Takahashi R, Ichita H, Tamura J, Kimura M, Ichinose M, Futami M-O, et al. Efficiency calculation of wind turbine generation system with doubly fed induction generator. In: Proceedings of the 19th international conference on electrical machines, September 6−8, 2010, Rome, Italy.

[26] Poore R, Lettenmaier T. Alternative design study report: windPACT advanced wind turbine drive train designs study. Golden, Colorado: NREL; August 2003. Report no. NREL/SR-500-33196.

[27] Giuffrida A, Ficarella A, Laforgia D. Study of the delivery behaviour of a pump for common rail fuel injection equipment. Proc Inst Mech Eng Part I J Syst Control Eng 2009;223(4):521−35. http://dx.doi.org/10.1243/09596518JSCE612.

[28] Manring ND. The discharge flow ripple of an axial-piston swash-plate type hydrostatic pump. ASME J Dyn Syst Meas Control 2000;122(2):263–8. http://dx.doi.org/10.1115/1.482452.

[29] Hibi A, Ichikawa T. Mathematical model of the torque characteristics for hydraulic motors. Bull JSME 1977;20(143):616–21.

[30] Merrill KJ, Holland MA, Lumkes JH. Efficiency analysis of a digital pump/motor as compared to a valve plate design. In: Proceedings of 7th international fluid power conference, March 22–24, 2010, Aachen, Germany.

[31] Muyeen SM. Wind power. Intech; 2010.